

SUPPLEMENTARY MATERIALS

4 in 1: multifunctional europium-organic framework with luminescent sensing properties, white light emission, proton conductivity and reverse acetylene-carbon dioxide adsorption selectivity

Xiaolin Yu ^{a,b}, Alexey A. Ryadun ^b, Konstantin A. Kovalenko ^b, Tatiana Y. Guselnikova ^b, Valentina G. Ponomareva ^c, Andrei S. Potapov ^{a,b}, Vladimir P. Fedin ^{a,b *}

^a Novosibirsk State University, 2 Pirogov Str. 630090, Novosibirsk, Russia

^b Nikolaev Institute of Inorganic Chemistry, Siberian Branch of the Russian Academy of Sciences, 3 Lavrentiev Ave., 630090, Novosibirsk, Russia

^c Institute of Solid State Chemistry and Mechanochemistry, Siberian Branch of the Russian Academy of Sciences, 18 Kutateladze Str. 630090, Novosibirsk, Russia

1. Supplementary figures

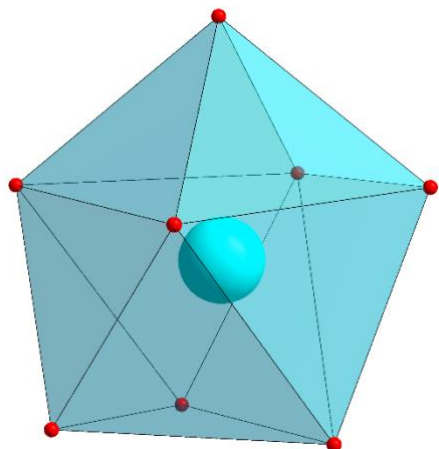


Figure S1. The coordination environment of Eu^{3+} ion.

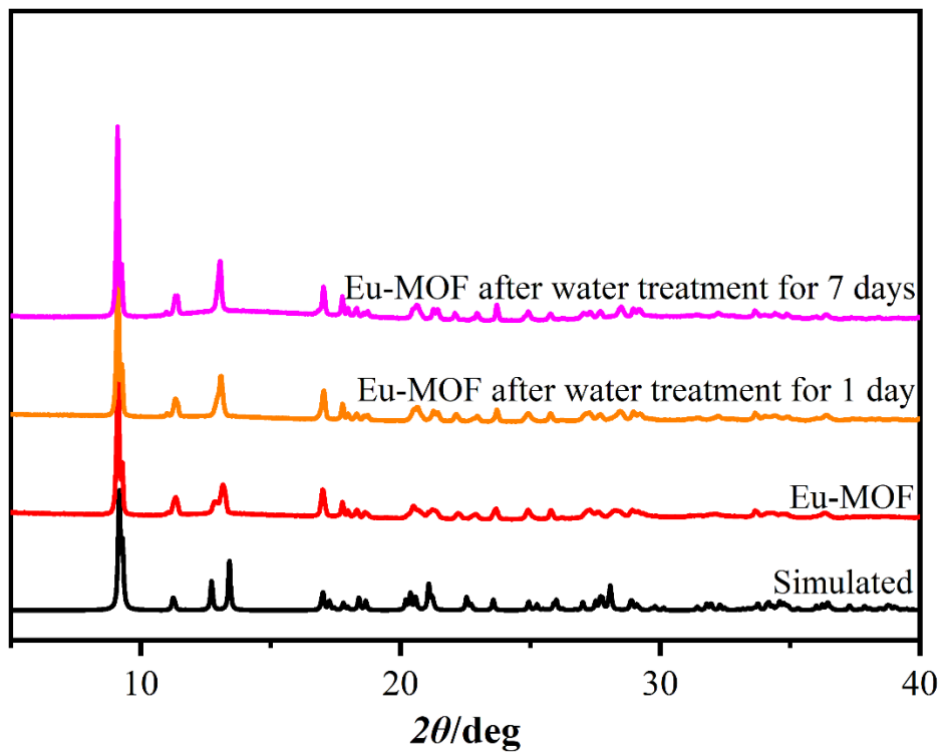


Figure S2. PXRD patterns of **Eu-MOF** bulk product (red) and Eu-MOF powder after immersion in water treatment for 1 day (orange) and 7 days (magenta) at 25 °C.

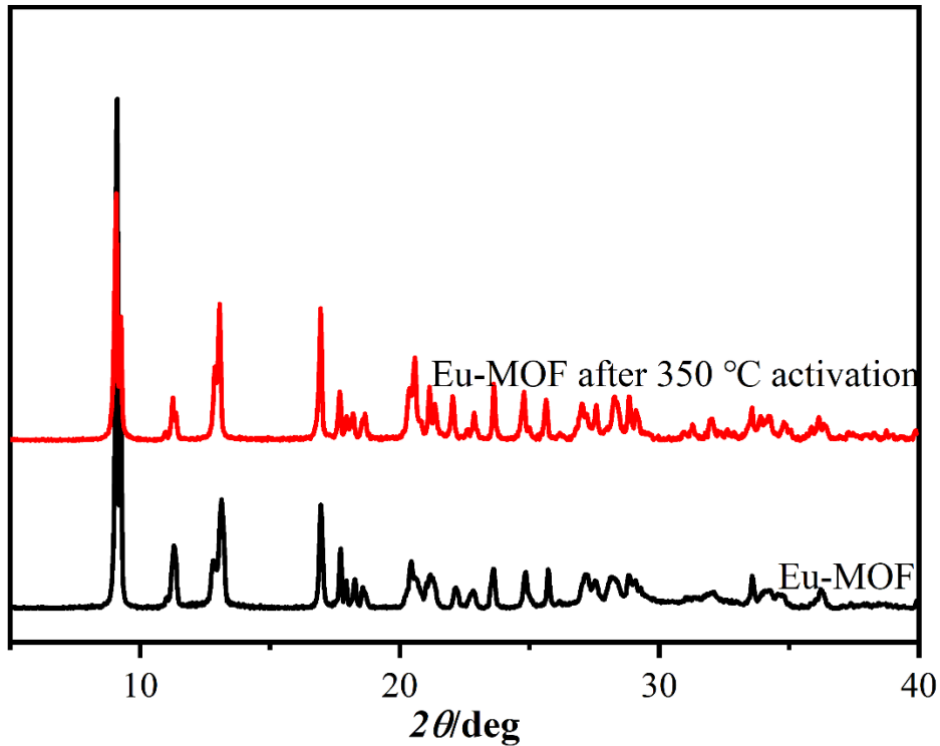


Figure S3. PXRD patterns of **Eu-MOF** after activation at 350 °C.

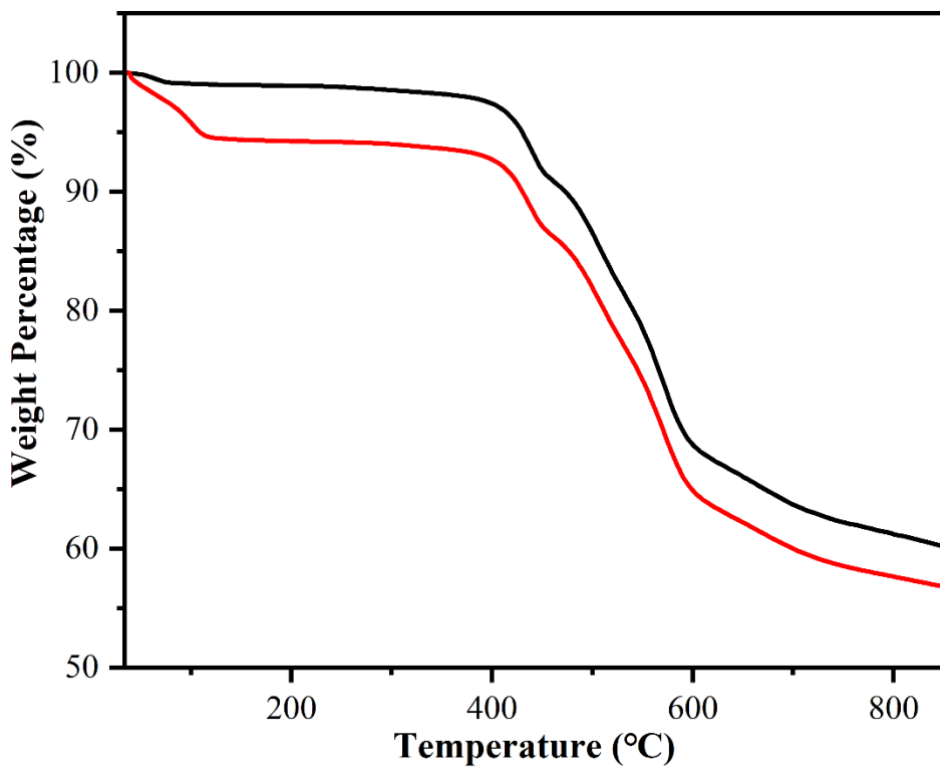
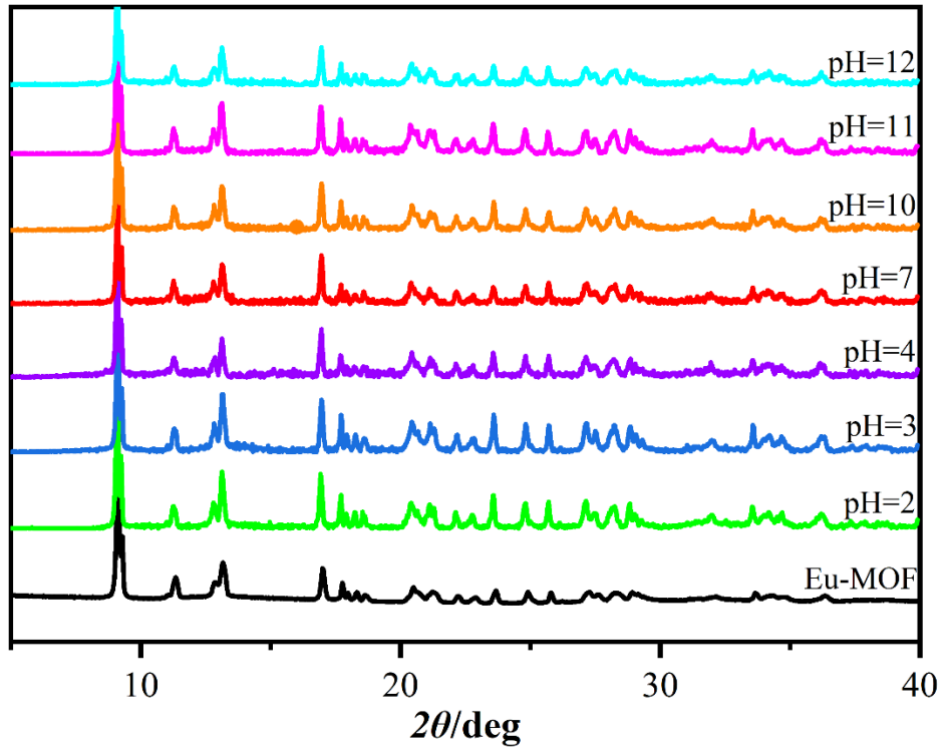
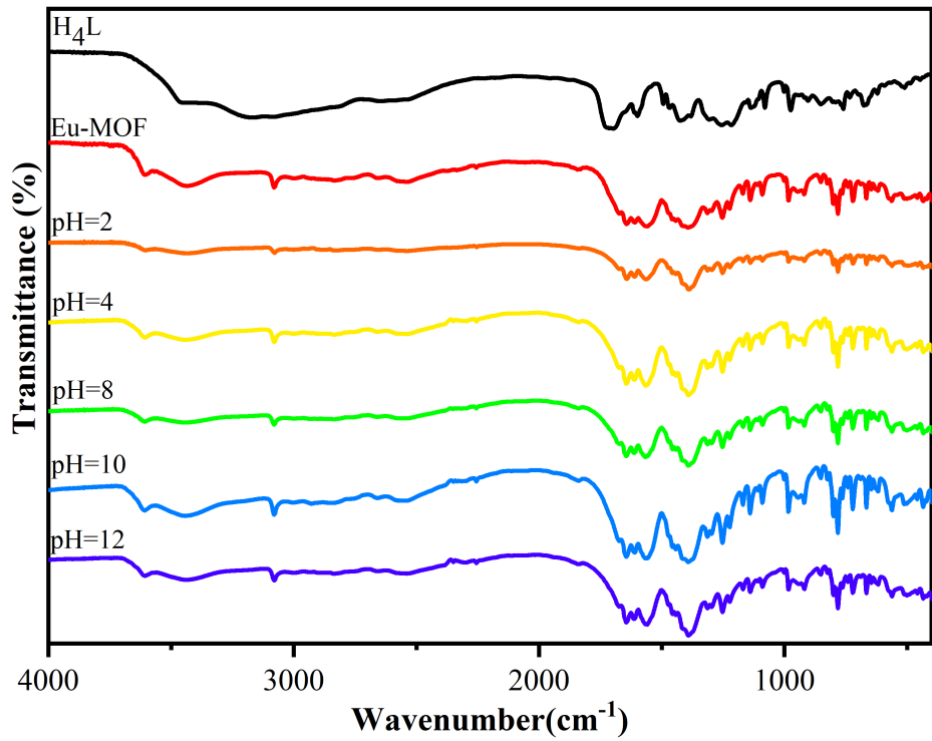


Figure S4. TGA plots of **Eu-MOF** under helium atmosphere after removal of coordinated and solvate water and acetonitrile molecules (black) and after standing in the air at room temperature for 10 days (red)



(a)



(b)

Figure S5. PXRD patterns (a) and FT-IR spectra (b) of **Eu-MOF** after soaking in aqueous solutions at different pH for 3 h at 25 °C.

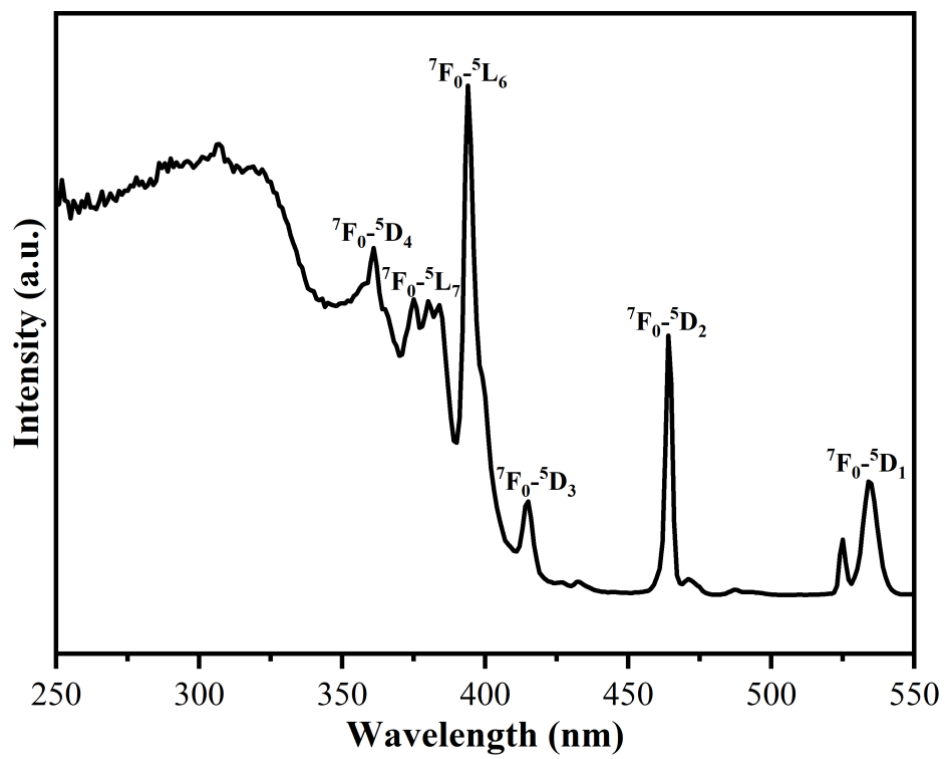


Figure S6. Solid state excitation spectrum of **Eu-MOF**.

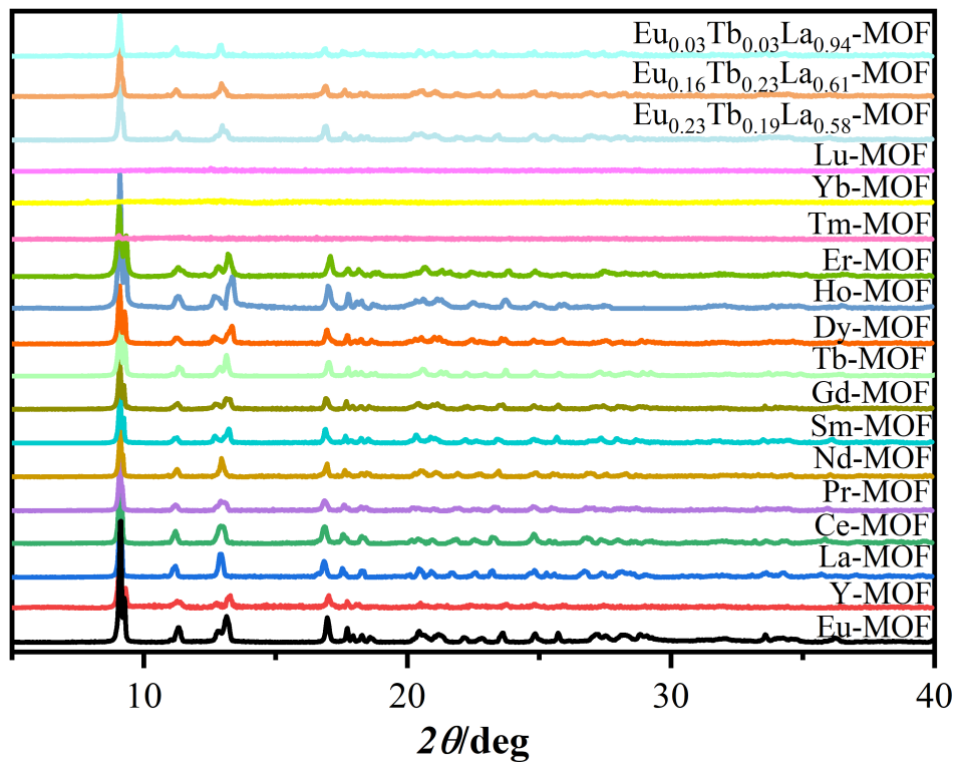


Figure S7. PXRD patterns of a series of lanthanide MOFs.

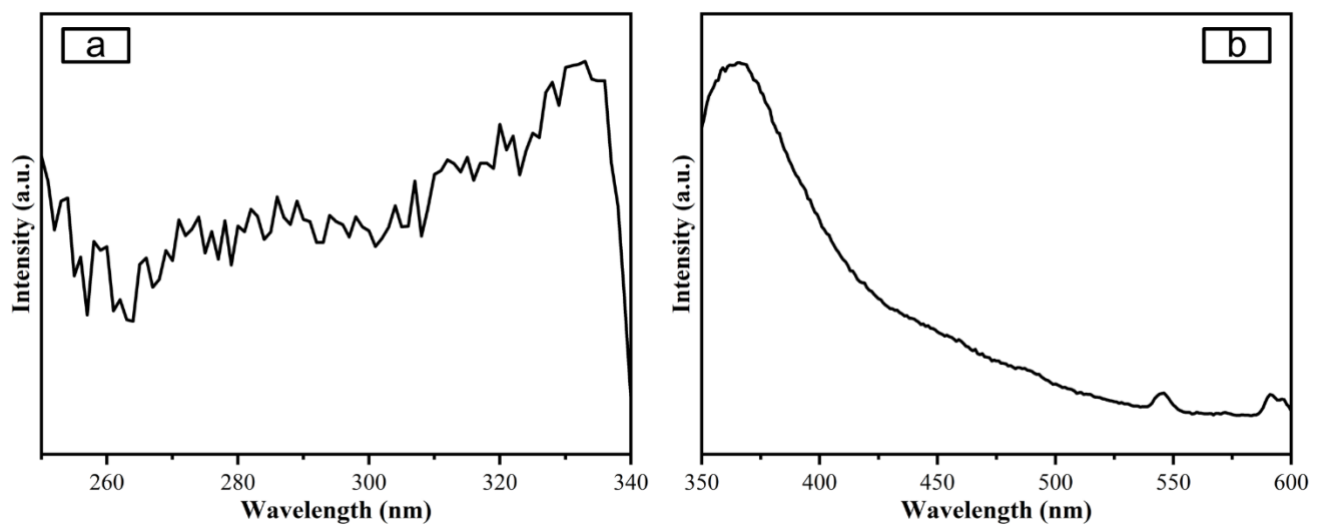


Figure S8. Solid state excitation (a) and emission (b, $\lambda_{\text{ex}} 330 \text{ nm}$) spectra of **La-MOF**.

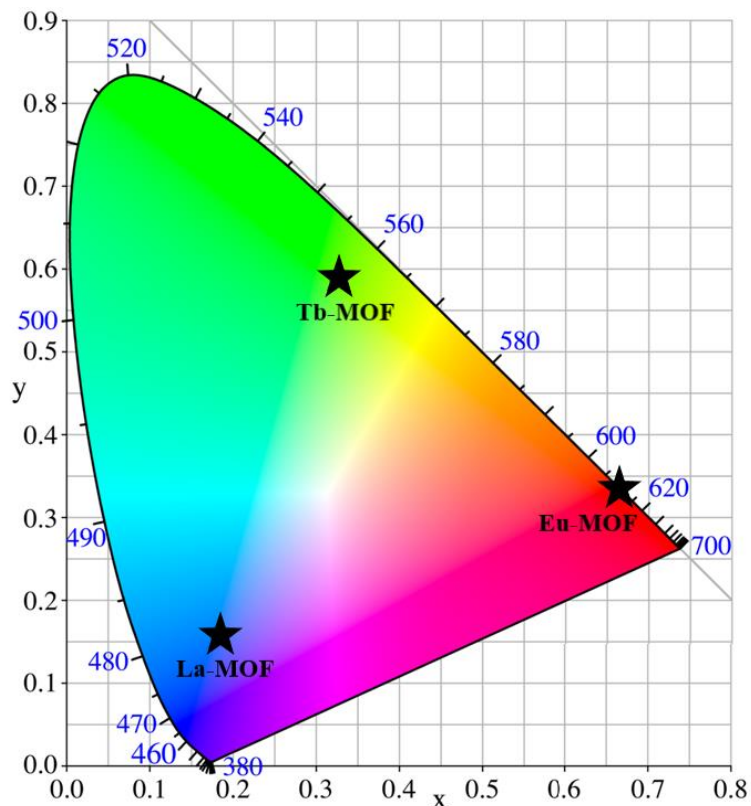


Figure S9. CIE-1931 chromaticity diagram for emission of **La-MOF** ($\lambda_{\text{ex}}=330 \text{ nm}$), **Eu-MOF** ($\lambda_{\text{ex}}=320 \text{ nm}$) and **Tb-MOF** ($\lambda_{\text{ex}}=320 \text{ nm}$).

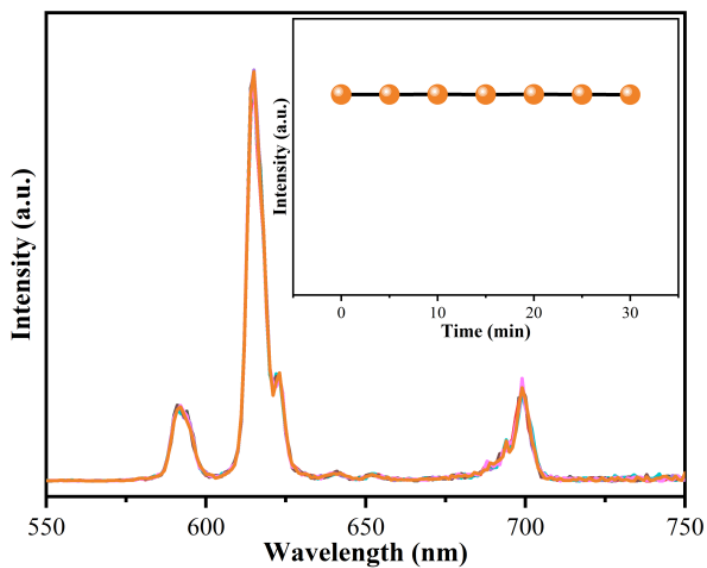


Figure S10. Emission spectra of aqueous suspension of **Eu-MOF** ($\lambda_{\text{ex}}=320 \text{ nm}$) recorded at 5 minutes intervals. Inset shows the independence of 625 nm peak intensity from time.

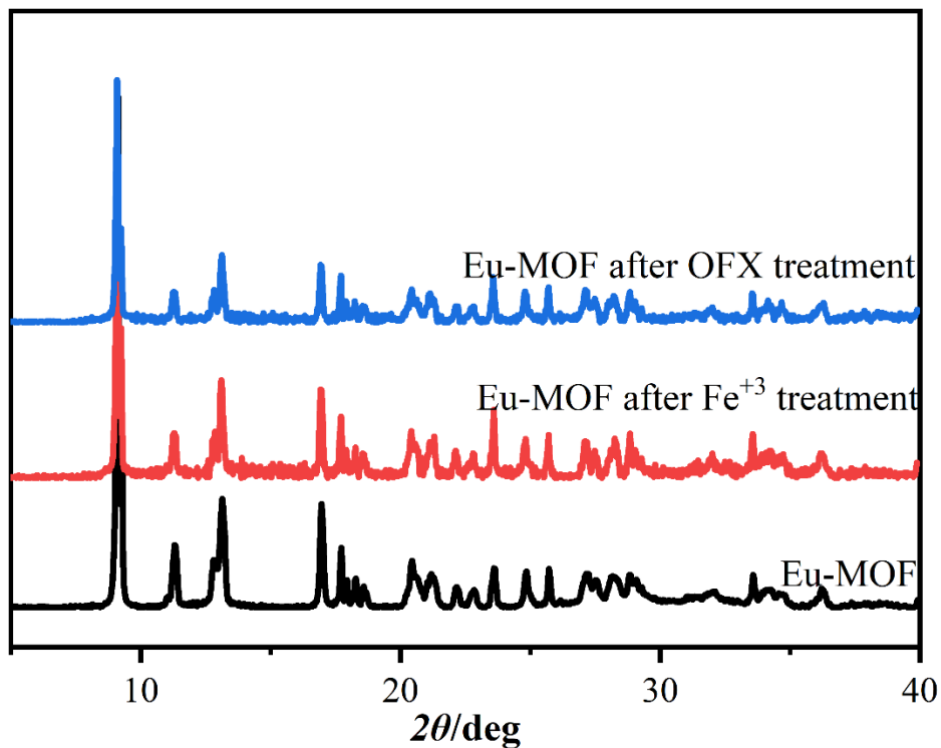


Figure S11. PXRD patterns of Eu-MOF after Fe^{3+} ($C = 10^{-4} \text{ M}$) treatment for 3 hours.

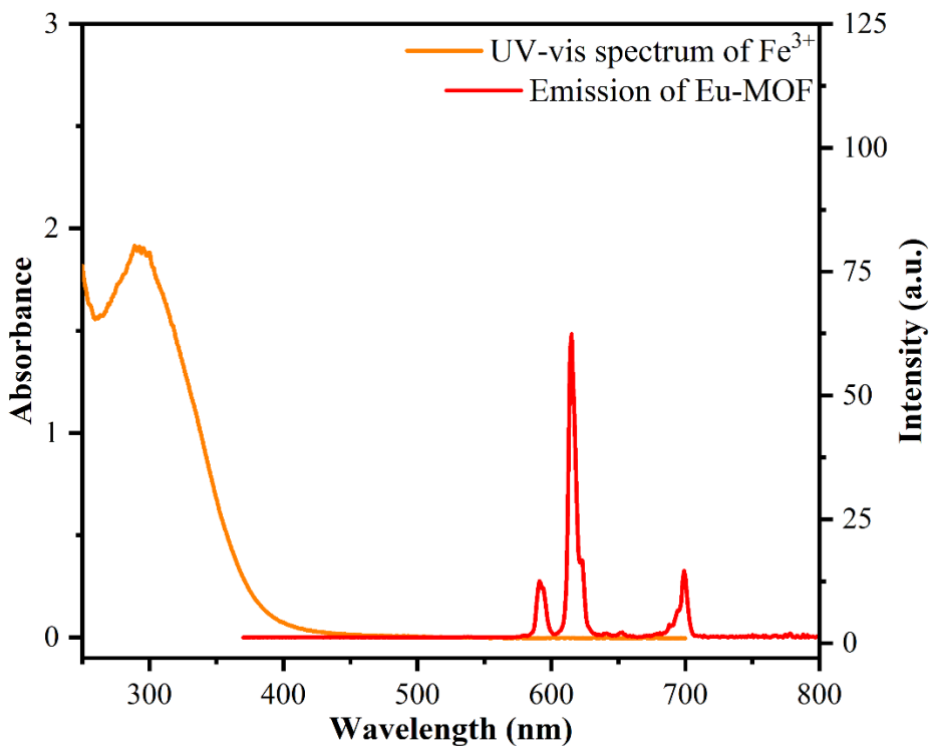


Figure S12. The UV–vis spectrum of Fe^{3+} ($C = 10^{-4}$ M) and emission spectra of **Eu-MOF** in water suspension

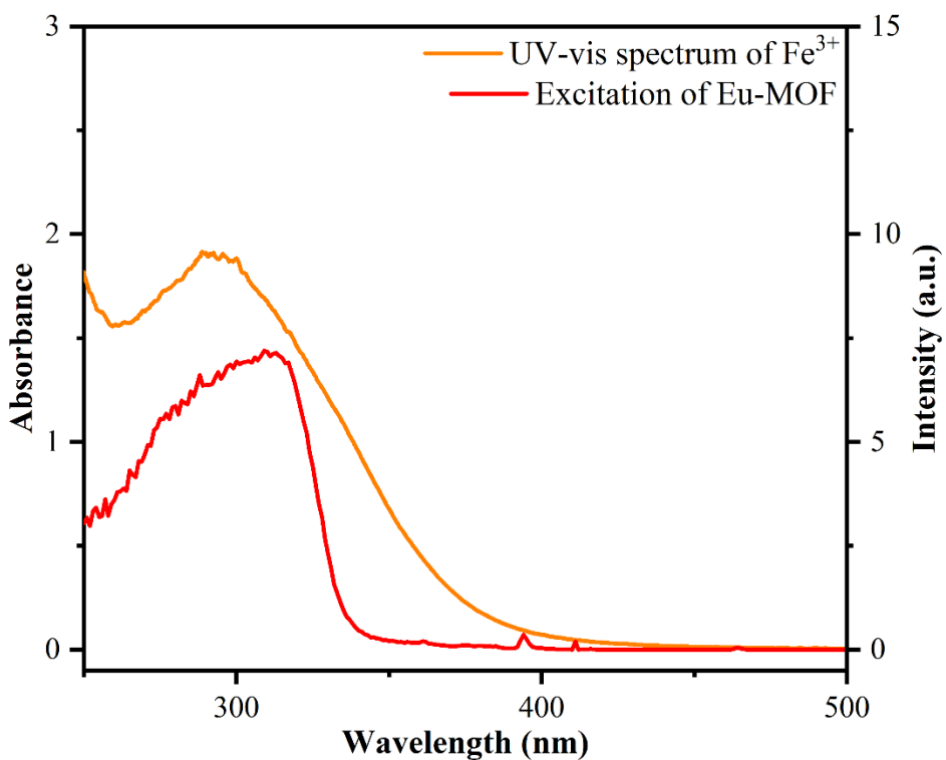


Figure S13. The UV–vis spectrum of Fe^{3+} ($C = 10^{-4}$ M) and excitation spectra of **Eu-MOF** in water suspension.

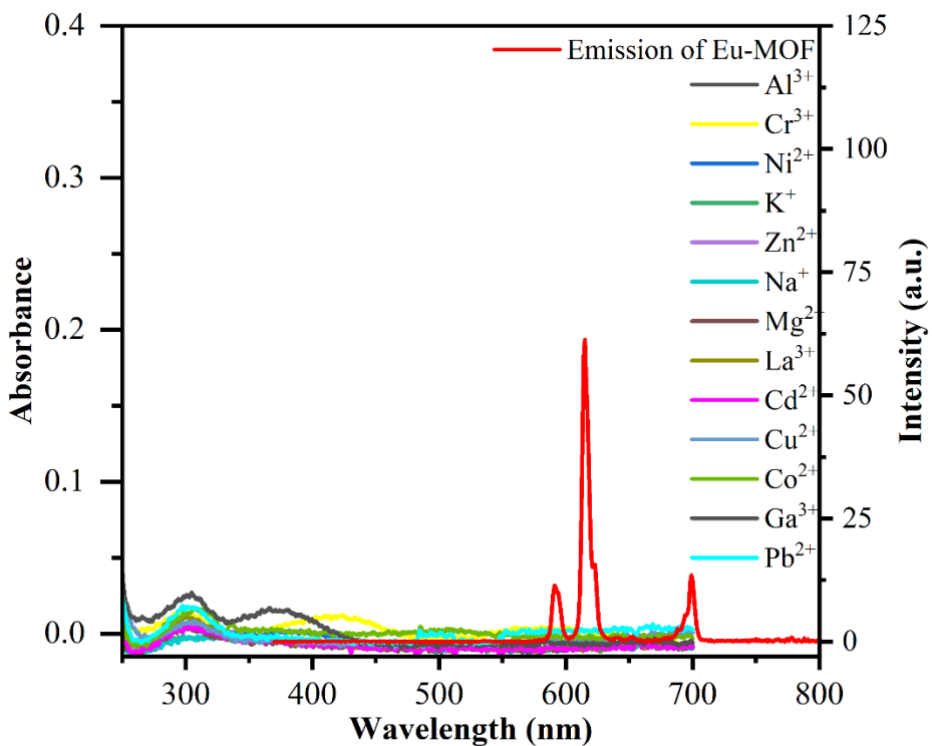


Figure S14. The UV–vis spectrum of the interfering ions ($C = 10^{-4}$ M) and emission spectra of Eu-MOF in water suspension.

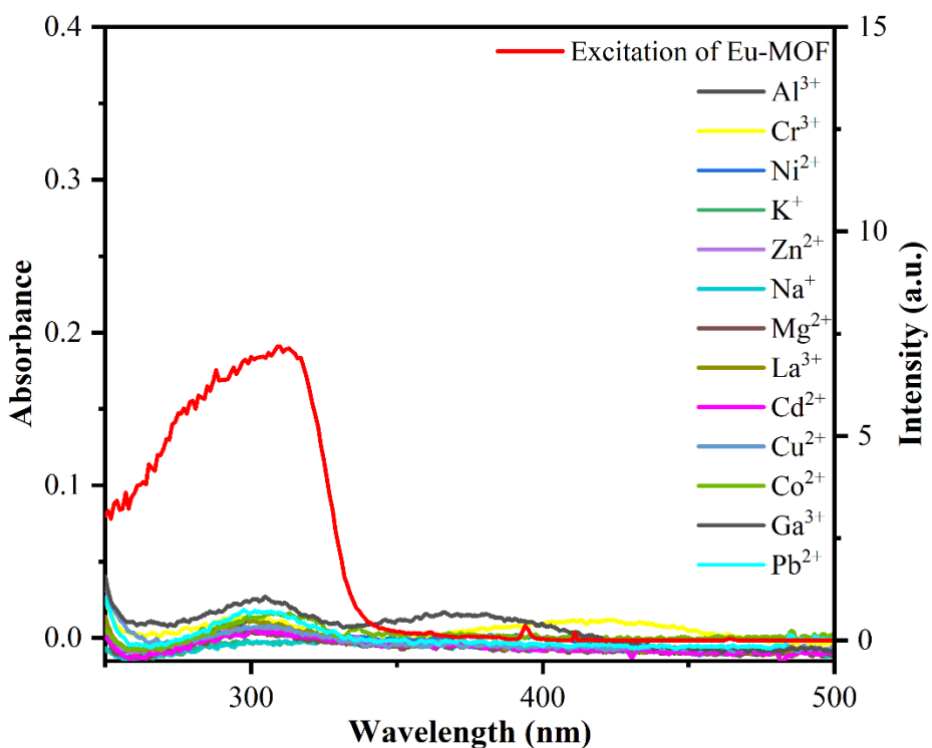


Figure S15. The UV–vis spectrum of the interfering ions ($C = 10^{-4}$ M) and excitation spectra of Eu-MOF in water suspension.

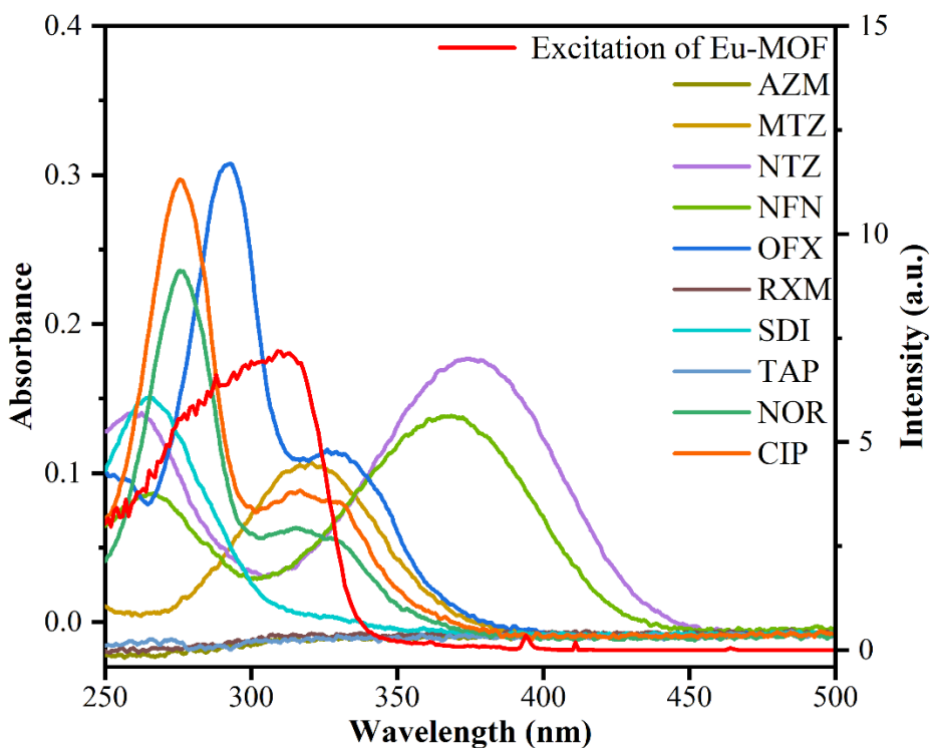


Figure S16. The UV–vis spectra of antibiotics ($C = 10^{-5}$ M) and the excitation spectrum of Eu-MOF.

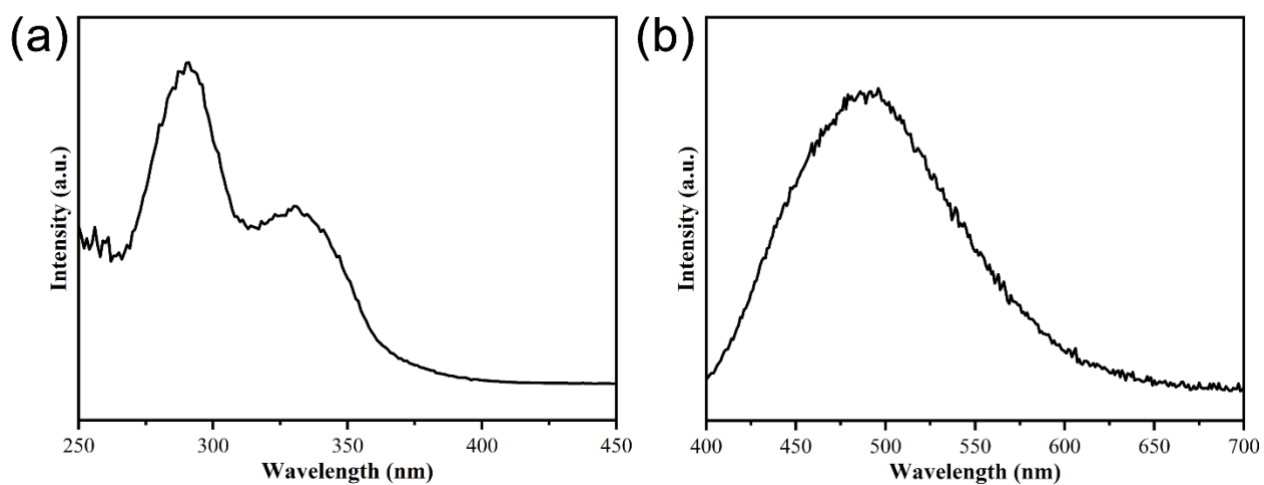


Figure S17. Excitation spectrum (a) and emission spectrum (b) of OFX solution ($C_{OFX} = 10^{-5}$ M).

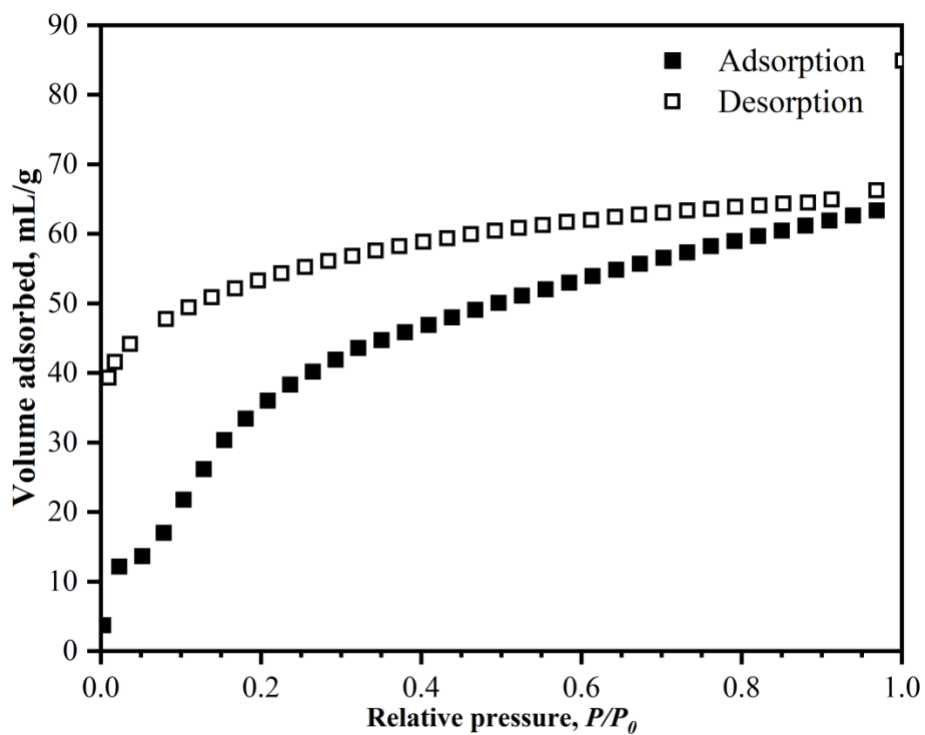


Figure S18. Carbon dioxide adsorption-desorption isotherms at 195 K.

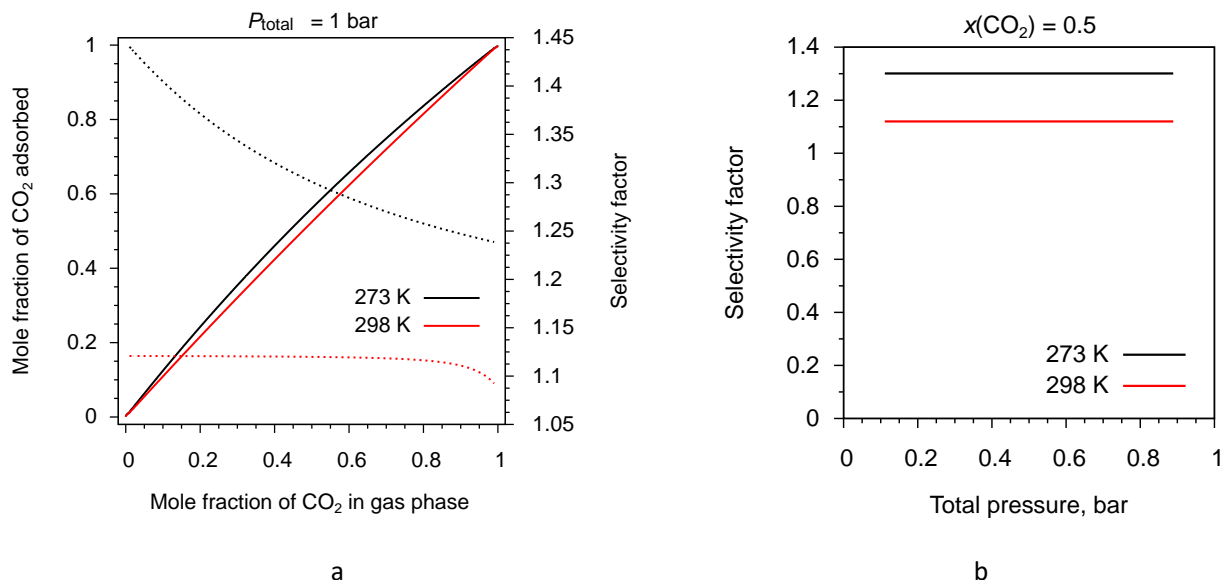


Figure S19. a) Prediction of adsorption equilibrium by IAST (solid lines) and dependence of selectivity factor on gas phase composition (dashed lines) at total pressure of $\text{CO}_2/\text{C}_2\text{H}_2$ mixture of 1 bar; b) dependence of selectivity factor on total pressure of equimolar binary $\text{CO}_2/\text{C}_2\text{H}_2$ mixture.

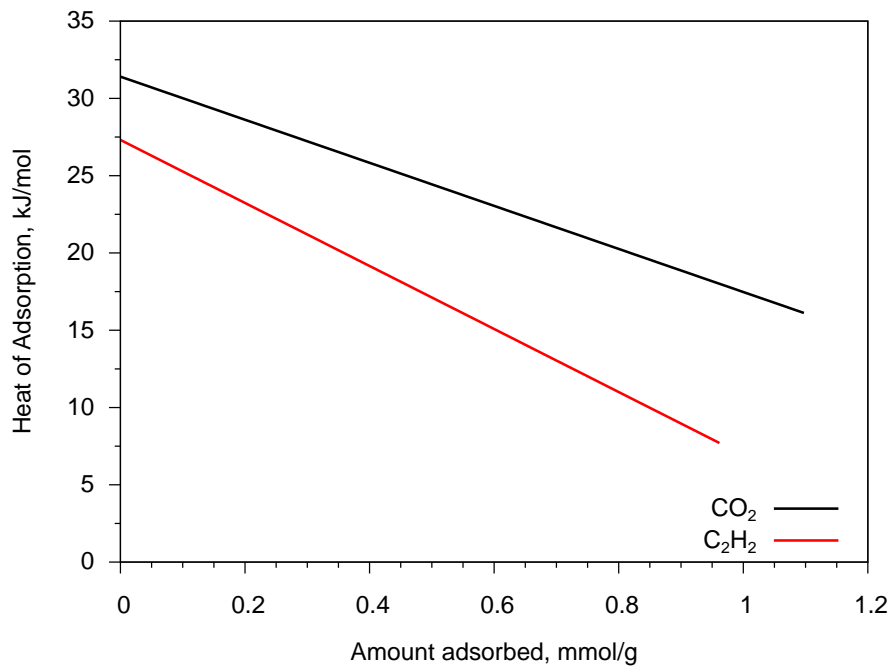


Figure S20. Isosteric heats of CO_2 and C_2H_2 adsorption on **Eu-MOF**.

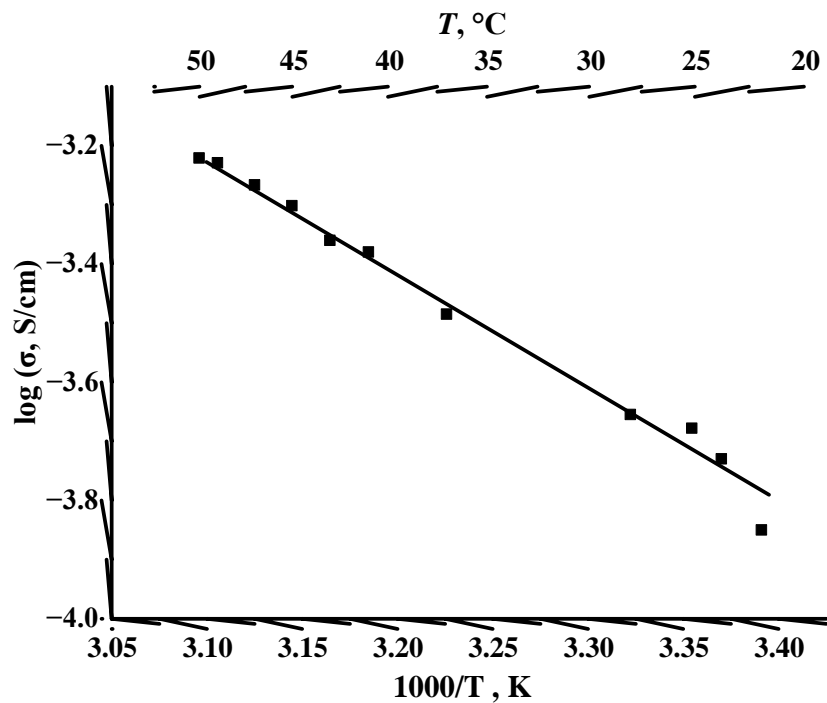


Figure S21. Temperature dependence of proton conductivity of **Eu-MOF** at $\text{RH} = 100\%$.

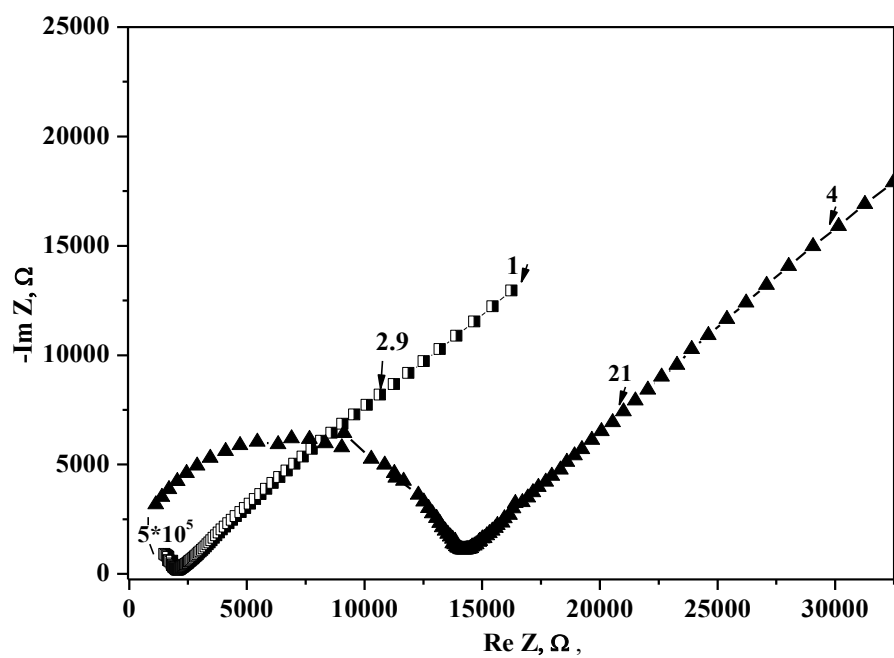


Figure S22. Impedance spectra of Eu-MOF at low (squares) and high (triangles) relative humidity. The values on graphs show the corresponding AC frequencies.

2. Supplementary tables

Table S1. Crystal data and structure refinements for **Eu-MOF**

Compound	Eu-MOF
Molecular formula	C ₁₇ H ₁₁ EuN _{0.5} O _{10.25}
Formula weight, g·mol ⁻¹	538.22
Temperature, K	150(2)
Crystal system	triclinic
Space group	P-1
a, Å	9.5701(9)
b, Å	10.5245(10)
c, Å	10.6495(8)
α, °	81.949(3)
β, °	64.876(3)
γ, °	65.100(3)
Cell volume, Å	879.89(14)
Z	2
ρ _{calc} , g/cm ³	2.031
μ, mm ⁻¹	3.624
F(000)	523.0
Independent reflections	3297 [R _{int} = 0.1097, R _{sigma} = 0.1195]
Goodness-of-fit on F ²	0.983
Final R indexes [I ≥ 2σ(I)]	R ₁ = 0.0558, wR ₂ = 0.1215
Final R indexes [all data]	R ₁ = 0.0832, wR ₂ = 0.1330

Table S2. Selected bond lengths (\AA) and angles ($^\circ$) for Eu-MOF

Eu1—O1M	2.548 (6)	Eu1—O16 ⁱⁱⁱ	2.366 (7)
Eu1—O11	2.315 (6)	Eu1—O17 ^{iv}	2.434 (6)
Eu1—O12 ⁱ	2.360 (7)	Eu1—O18 ^v	2.373 (6)
Eu1—O13 ⁱⁱ	2.575 (7)	Eu1—O19 ^{vi}	2.360 (7)
O1M—Eu1—Eu1 ⁱ	109.15 (16)	O12 ⁱ —Eu1—O18 ^v	140.3 (2)
O1M—Eu1—O13 ⁱⁱ	127.3 (2)	O12 ⁱ —Eu1—O19 ^{vi}	84.5 (2)
O1M—Eu1—C9 ^{iv}	135.9 (2)	O12 ⁱ —Eu1—C9 ^{iv}	75.8 (2)
O11—Eu1—Eu1 ⁱ	61.56 (17)	O13 ⁱⁱ —Eu1—Eu1 ⁱ	123.51 (17)
O11—Eu1—O1M	69.6 (2)	O13 ⁱⁱ —Eu1—C9 ^{iv}	83.1 (2)
O11—Eu1—O12 ⁱ	125.1 (2)	O16 ⁱⁱⁱ —Eu1—Eu1 ⁱ	46.39 (17)
O11—Eu1—O13 ⁱⁱ	137.7 (2)	O16 ⁱⁱⁱ —Eu1—O1M	75.0 (2)
O11—Eu1—O16 ⁱⁱⁱ	75.7 (2)	O16 ⁱⁱⁱ —Eu1—O13 ⁱⁱ	141.7 (2)
O11—Eu1—O17 ^{iv}	72.6 (2)	O16 ⁱⁱⁱ —Eu1—O17 ^{iv}	121.4 (2)
O11—Eu1—O18 ^v	83.5 (2)	O16 ⁱⁱⁱ —Eu1—O18 ^v	145.6 (2)
O11—Eu1—O19 ^{vi}	141.4 (2)	O17 ^{iv} —Eu1—Eu1 ⁱ	75.17 (17)
O11—Eu1—C9 ^{iv}	67.0 (2)	O17 ^{iv} —Eu1—O1M	132.8 (2)
O12 ⁱ —Eu1—Eu1 ⁱ	64.20 (17)	O17 ^{iv} —Eu1—O13 ⁱⁱ	69.6 (2)
O12 ⁱ —Eu1—O1M	139.3 (2)	O17 ^{iv} —Eu1—C9 ^{iv}	20.5 (2)
O12 ⁱ —Eu1—O13 ⁱⁱ	70.7 (2)	O18 ^v —Eu1—Eu1 ⁱ	140.08 (17)
O12 ⁱ —Eu1—O16 ⁱⁱⁱ	73.6 (2)	O18 ^v —Eu1—O1M	72.1 (2)
O12 ⁱ —Eu1—O17 ^{iv}	86.2 (2)	O18 ^v —Eu1—O13 ⁱⁱ	69.8 (2)
O18 ^v —Eu1—O17 ^{iv}	76.4 (2)	C9 ^{iv} —Eu1—Eu1 ⁱ	54.81 (19)
O18 ^v —Eu1—C9 ^{iv}	95.4 (2)	C1—O11—Eu1	147.1 (7)
O19 ^{vi} —Eu1—Eu1 ⁱ	132.73 (16)	C1—O12—Eu1 ⁱ	137.2 (6)
O19 ^{vi} —Eu1—O1M	71.8 (2)	C8—O13—Eu1 ^{vii}	134.9 (7)
O19 ^{vi} —Eu1—O13 ⁱⁱ	70.8 (2)	C5—O15—C15	113.5 (8)
O19 ^{vi} —Eu1—O16 ⁱⁱⁱ	92.7 (2)	C9—O16—Eu1 ⁱⁱⁱ	175.8 (7)
O19 ^{vi} —Eu1—O17 ^{iv}	140.1 (2)	C9—O17—Eu1 ^{viii}	116.6 (6)
O19 ^{vi} —Eu1—O18 ^v	86.5 (2)	C10—O18—Eu1 ^v	142.9 (6)
O19 ^{vi} —Eu1—C9 ^{iv}	151.4 (2)	C10—O19—Eu1 ^{ix}	143.8 (6)

Symmetry codes: (i) $-x+1, -y, -z$; (ii) $x+1, y, z-1$; (iii) $-x+1, -y, -z+1$; (iv) $x, y, z-1$; (v) $-x+1, -y+1, -z+1$; (vi) $x+1, y-1, z-1$; (vii) $x-1, y, z+1$; (viii) $x, y, z+1$; (ix) $x-1, y+1, z+1$.

Table S3. ICP-AES analysis results of trimetallic MOFs

Compound	Eu content, mol. %	Tb content, mol. %	La content, mol. %
Eu _{0.23} Tb _{0.19} La _{0.58} -MOF	23.0	19.5	57.5
Eu _{0.16} Tb _{0.23} La _{0.61} -MOF	16.0	22.7	61.3
Eu _{0.03} Tb _{0.03} La _{0.94} -MOF	3.3	2.7	94.0

Table S4. CIE color coordinates, absolute quantum yields and luminescence lifetimes for
Tb-MOF, La-MOF and trimetallic Eu_xTb_yLa_{1-x-y} MOFs

compounds	CIE coordinates	ψ (%)	τ (ms)	λ_{ex} (nm)	λ_{em} (nm)
Tb-MOF	(0.33, 0.59)	44	1.16	320	545
La-MOF	(0.18, 0.15)			330	360
Eu _{0.23} Tb _{0.19} La _{0.58} -MOF	(0.56, 0.41)			325	545
Eu _{0.16} Tb _{0.23} La _{0.61} -MOF	(0.49, 0.45)			325	545
Eu _{0.03} Tb _{0.03} La _{0.94} -MOF	(0.45, 0.47)			320	546
Eu _{0.03} Tb _{0.03} La _{0.94} -MOF	(0.39, 0.43)			340	543
Eu _{0.03} Tb _{0.03} La _{0.94} -MOF	(0.36, 0.40)			360	544
Eu _{0.03} Tb _{0.03} La _{0.94} -MOF	(0.35, 0.38)			364	545
Eu _{0.03} Tb _{0.03} La _{0.94} -MOF	(0.34, 0.37)			368	543
Eu _{0.03} Tb _{0.03} La _{0.94} -MOF	(0.33, 0.36)			372	543
Eu _{0.03} Tb _{0.03} La _{0.94} -MOF	(0.31, 0.32)	5		380	543

Table S5. The parameters of porous structure of Eu-MOF.

Specific surface area, m ² ·g ⁻¹		V_{pore} , cm ³ ·g ⁻¹		$V_{\text{ads}}(\text{N}_2)^a$, cm ³ (STP)·g ⁻¹	
Langmuir	BET	DFT	Total ^a	DFT	
—	142.7	84.5	0.098	0.093	62.5

^a measured at $P/P_0 = 0.95$.

Table S6. Selectivity factors for separation of equimolar binary CO₂/C₂H₂ mixture.

Calculation method	273 K	298 K
Amount adsorbed ratio	1.3	1.1
Henry constants ratio	1.5	1.3
IAST	1.3	1.1

Table S7. Comparison of CO₂ and C₂H₂ uptakes and adsorption selectivity factors for the representative CO₂/C₂H₂ selective MOFs at 1 bar.

Material ^a	<i>T</i> , K	CO ₂ uptake,	C ₂ H ₂ uptake,	Selectivity		Ref.
		mL(STP)·g ⁻¹	mL(STP)·g ⁻¹	IAST	V ₁ /V ₂	
[Cu(PF ₆) ₂ (bpetha) ₂]	195	135	78	n/a	1.73	¹
[Zn ₂ (bdc) ₂ (dabco)] ^b DSB	195	140	73	n/a	1.92	²
K ₂ [Cr ₃ O(O ₂ CH) ₆ (4-Etpy) ₃] ₂ [α -SiW ₁₂ O ₄₀]	278	12	2.5	n/a	4.8	³
[Co(HL ^d c)]	195	239.5	140	1.7	1.7	⁴
[Mn(bdc)(dpe)]	273	15.7 ^b / 47.1	2.2 ^b / 6.7	13 ^c / 8.8	7.0	⁵
SIFSIX-3-Ni	298	56.0 ^c / 60.5	47.1 ^c / 74.0	14.3 ^c / 7.7 ^d	0.82	⁶
NbOFFIVE-1-Ni	298	3 / 49.3	13 ^b / 53.8	n/a	0.9	⁷
CD-MOF-1	298	12.3 ^e / 64.3	3.4 ^e / 50.0	6.6 ^d	1.3	⁸
CD-MOF-2	298	24.6 ^e / 59.4	0.7 ^e / 45.5	16.0 ^d	1.3	
[Tm ₂ (OH-bdc) ₂ (μ_3 -OH) ₂ (H ₂ O) ₂]	298	4.3 ^e / 130.7	0.2 ^e / 47.1	17.5 ^d	2.8	⁹
[Tm ₂ (OH-bdc) ₂ (μ_3 -OH) ₂]	298	1.1 ^e / 139.2	0.7 ^e / 117.7	1.65 ^d	1.2	
Cd[Fe(CN) ₅ (NO)]	298	58	9.7	85	6.0	¹⁰
MUF-16(Co)	293	48	4.0	510	12	
MUF-16(Mn)	293	50.5	9.7	31	5.2	¹¹
MUF-16(Ni)	293	48	7.5	46	6.4	
[Sc(Hpzc)(pzc)]	273	48.9	14.9	2.1	3.28	¹²
	298	11.9	7.3	1.1	1.63	
[Zn(atz)(bdc-Cl ₄) _{0.5}]	285	21	10.9	2.4	1.9	¹³
Eu-MOF	273	32.7	25.6	1.3	1.3	This
	298	23.3	20.7	1.1	1.1	work

^a bpetha = 1,2-bis(4-pyridyl)ethane; bdc²⁻ = 1,4-benzenedicarboxylate; dabco = 1,4-diazabicyclo[2.2.2]octane; DSB = distyrylbenzene; 4-Etpy = 4-ethylpyridine; dpe = 1,2-di(4-pyridyl)ethylene; OH-bdc²⁻ = 2,5-dihydroxyterephthalate; H₂pzc = 2,5-pyrazinedicarboxylic acid; Hatz = 3-amino-1,2,4-triazole; bdc-Cl₄²⁻ = tetrachloroterephthalate;

^b at 0.1 bar;

^c IAST selectivity at total pressure 0.15 bar for 1:1 gas mixture;

^d IAST selectivity at total pressure 1 bar for C₂H₂/CO₂ = 1:2 gas mixture;

^e at 0.2 bar.

References

- (1) Noro, S.; Tanaka, D.; Sakamoto, H.; Shimomura, S.; Kitagawa, S.; Takeda, S.; Uemura, K.; Kita, H.; Akutagawa, T.; Nakamura, T. Selective Gas Adsorption in One-Dimensional, Flexible Cull Coordination Polymers with Polar Units. *Chem. Mater.* **2009**, 21 (14), 3346–3355. <https://doi.org/10.1021/cm9012969>.

- (2) Yanai, N.; Kitayama, K.; Hijikata, Y.; Sato, H.; Matsuda, R.; Kubota, Y.; Takata, M.; Mizuno, M.; Uemura, T.; Kitagawa, S. Gas Detection by Structural Variations of Fluorescent Guest Molecules in a Flexible Porous Coordination Polymer. *Nature Mater.* **2011**, *10* (10), 787–793. <https://doi.org/10.1038/nmat3104>.
- (3) Eguchi, R.; Uchida, S.; Mizuno, N. Inverse and High CO₂/C₂H₂ Sorption Selectivity in Flexible Organic–Inorganic Ionic Crystals. *Angew. Chem. Int. Ed.* **2012**, *51* (7), 1635–1639. <https://doi.org/10.1002/anie.201107906>.
- (4) Yang, W.; Davies, A. J.; Lin, X.; Suyetin, M.; Matsuda, R.; Blake, A. J.; Wilson, C.; Lewis, W.; Parker, J. E.; Tang, C.; George, M. W.; Hubberstey, P.; Kitagawa, S.; Sakamoto, H.; Bichoutskaia, E.; Champness, N. R.; Yang, S.; Schröder, M. Selective CO₂ Uptake and Inverse CO₂/C₂H₂ Selectivity in a Dynamic Bifunctional Metal–Organic Framework. *Chem. Sci.* **2012**, *3* (10), 2993. <https://doi.org/10.1039/c2sc20443f>.
- (5) Foo, M. L.; Matsuda, R.; Hijikata, Y.; Krishna, R.; Sato, H.; Horike, S.; Hori, A.; Duan, J.; Sato, Y.; Kubota, Y.; Takata, M.; Kitagawa, S. An Adsorbate Discriminatory Gate Effect in a Flexible Porous Coordination Polymer for Selective Adsorption of CO₂ over C₂H₂. *J. Am. Chem. Soc.* **2016**, *138* (9), 3022–3030. <https://doi.org/10.1021/jacs.5b10491>.
- (6) Chen, K.-J.; Scott, H. S.; Madden, D. G.; Pham, T.; Kumar, A.; Bajpai, A.; Lusi, M.; Forrest, K. A.; Space, B.; Perry, J. J.; Zaworotko, M. J. Benchmark C₂H₂/CO₂ and CO₂/C₂H₂ Separation by Two Closely Related Hybrid Ultramicroporous Materials. *Chem* **2016**, *1* (5), 753–765. <https://doi.org/10.1016/j.chempr.2016.10.009>.
- (7) Belmabkhout, Y.; Zhang, Z.; Adil, K.; Bhatt, P. M.; Cadiou, A.; Solovyeva, V.; Xing, H.; Eddaoudi, M. Hydrocarbon Recovery Using Ultra-Microporous Fluorinated MOF Platform with and without Uncoordinated Metal Sites: I-Structure Properties Relationships for C₂H₂/C₂H₄ and CO₂/C₂H₂ Separation. *Chemical Engineering Journal* **2019**, *359*, 32–36. <https://doi.org/10.1016/j.cej.2018.11.113>.
- (8) Li, L.; Wang, J.; Zhang, Z.; Yang, Q.; Yang, Y.; Su, B.; Bao, Z.; Ren, Q. Inverse Adsorption Separation of CO₂/C₂H₂ Mixture in Cyclodextrin-Based Metal–Organic Frameworks. *ACS Appl. Mater. Interfaces* **2019**, *11* (2), 2543–2550. <https://doi.org/10.1021/acsami.8b19590>.
- (9) Ma, D.; Li, Z.; Zhu, J.; Zhou, Y.; Chen, L.; Mai, X.; Liufu, M.; Wu, Y.; Li, Y. Inverse and Highly Selective Separation of CO₂/C₂H₂ on a Thulium–Organic Framework. *J. Mater. Chem. A* **2020**, *8* (24), 11933–11937. <https://doi.org/10.1039/D0TA03151H>.
- (10) Xie, Y.; Cui, H.; Wu, H.; Lin, R.; Zhou, W.; Chen, B. Electrostatically Driven Selective Adsorption of Carbon Dioxide over Acetylene in an Ultramicroporous Material. *Angew. Chem. Int. Ed.* **2021**, *60* (17), 9604–9609. <https://doi.org/10.1002/anie.202100584>.
- (11) Qazvini, O. T.; Babarao, R.; Telfer, S. G. Selective Capture of Carbon Dioxide from Hydrocarbons Using a Metal–Organic Framework. *Nat Commun* **2021**, *12* (1), 197. <https://doi.org/10.1038/s41467-020-20489-2>.
- (12) Barsukova, M. O.; Kovalenko, K. A.; Nizovtsev, A. S.; Sapianik, A. A.; Samsonenko, D. G.; Dybtsev, D. N.; Fedin, V. P. Isomeric Scandium–Organic Frameworks with High Hydrolytic Stability and Selective Adsorption of Acetylene. *Inorg. Chem.* **2021**, *60* (5), 2996–3005. <https://doi.org/10.1021/acs.inorgchem.0c03159>.
- (13) Li, X.-Y.; Song, Y.; Zhang, C.-X.; Zhao, C.-X.; He, C. Inverse CO₂/C₂H₂ Separation in a Pillared-Layer Framework Featuring a Chlorine-Modified Channel by Quadrupole-Moment Sieving. *Separation and Purification Technology* **2021**, *279*, 119608. <https://doi.org/10.1016/j.seppur.2021.119608>.

3. Details of gas adsorption experiments

3.1. Heats of Adsorption

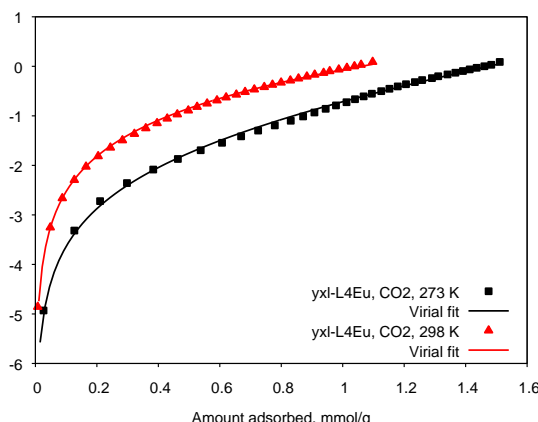
Gas adsorption isotherms at 273 K and 298 K were fitted by virial equation (S1) in order to calculate Henry constants and isosteric heats of adsorption.

$$\ln p = \ln n + \frac{1}{T} \sum_i A_i \cdot n^i + \sum_j B_j \cdot n^j \quad (\text{S1})$$

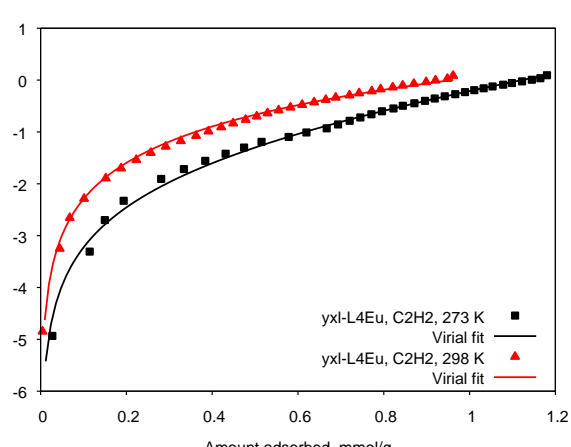
Virial coefficients are summarized in Table S6, whereas the fit plots are shown in Figure S22.

Table S8. Virial coefficients A_i and B_j for gas adsorption isotherms at 273 K and 298 K on Eu-MOF.

Gas	Coefficients
CO ₂	$A_0 = -3777.22 \pm 92.18$ (2.44%) $A_1 = 1675.64 \pm 110.5$ (6.592%) $B_0 = 12.4333 \pm 0.3213$ (2.584%) $B_1 = -5.44992 \pm 0.3923$ (7.198%)
C ₂ H ₂	$A_0 = -3284.84 \pm 181$ (5.51%) $A_1 = 2451.89 \pm 262.2$ (10.69%) $B_0 = 11.0279 \pm 0.6319$ (5.73%) $B_1 = -8.18871 \pm 0.9274$ (11.33%)



a



b

Figure S22. Fits of isotherms by virial equations for CO₂ (a) and C₂H₂ (b).

The isosteric heats of adsorption were calculated using virial coefficients by equation (S2):

$$\Delta H^\circ = R \cdot \sum_i A_i \cdot n^i \quad (\text{S2})$$

The corresponding graphs are shown in Figure S23.

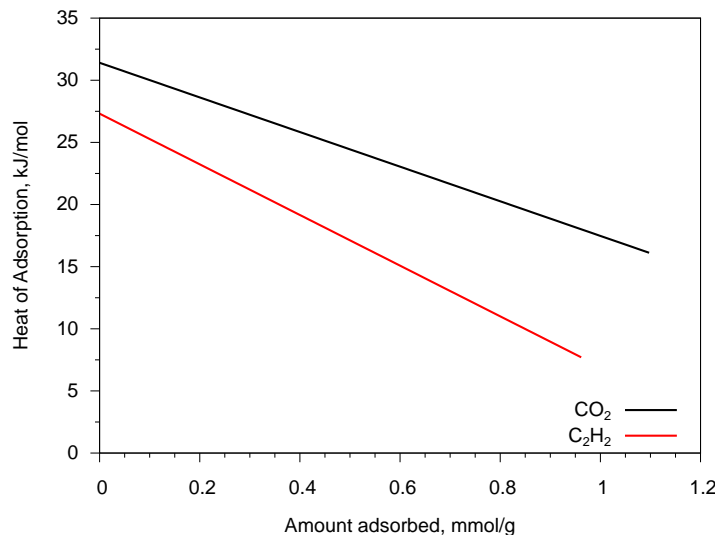


Figure S23. Isosteric heats of CO₂ and C₂H₂ adsorption on **Eu-MOF**.

3.2. Adsorption selectivity

The selectivity factors for separation of binary gas mixture C₂H₂/CO₂ were evaluated by three different methods: i) as ratio of amount adsorbed; ii) as ratio of corresponding Henry constants; and iii) by Ideal Adsorbed Solution Theory (IAST) calculations which possess to estimate selectivity factors at different gas mixture compositions and total pressures. The relationship between P , y_i and x_i (P — the total pressure of the gas phase, y_i — mole fraction of the i -component in gas phase, x_i — mole fraction of the i -component in absorbed state) is defined according to the IAST theory:

$$\int_{p=0}^{p=\frac{Py_1}{x_1}} n_1(p) d\ln p = \int_{p=0}^{p=\frac{Py_2}{x_2}} n_2(p) d\ln p, \quad (\text{S3})$$

where $n_i(p)$ — amount adsorbed at pressure p .

In this case the selectivity factors were determined as:

$$S = \frac{y_2 x_2}{y_1 x_1} = \frac{x_1(1-y_1)}{y_1(1-x_1)} \quad (\text{S4})$$

For IAST calculations adsorption isotherms were fitted by common Langmuir equation. Fittings were performed for isotherms in mL/g–torr units, so parameters are in the corresponding units. Fitted parameters are summarized in Table S7. The fitted isotherms are shown in Figure S24.

Table S9. Fitted parameters for adsorption isotherms on **Eu-MOF** at 273 K and 298 K

Gas	273 K	298 K
C ₂ H ₂	$w = 50.4 \pm 0.9$ $b = 0.00134 \pm 0.00004$	$w = 116 \pm 5$ $b = 0.000289 \pm 0.000016$
CO ₂	$w = 52.7 \pm 0.7$ $b = 0.00210 \pm 0.00005$	$w = 97.2 \pm 1.5$ $b = 0.000418 \pm 0.000008$

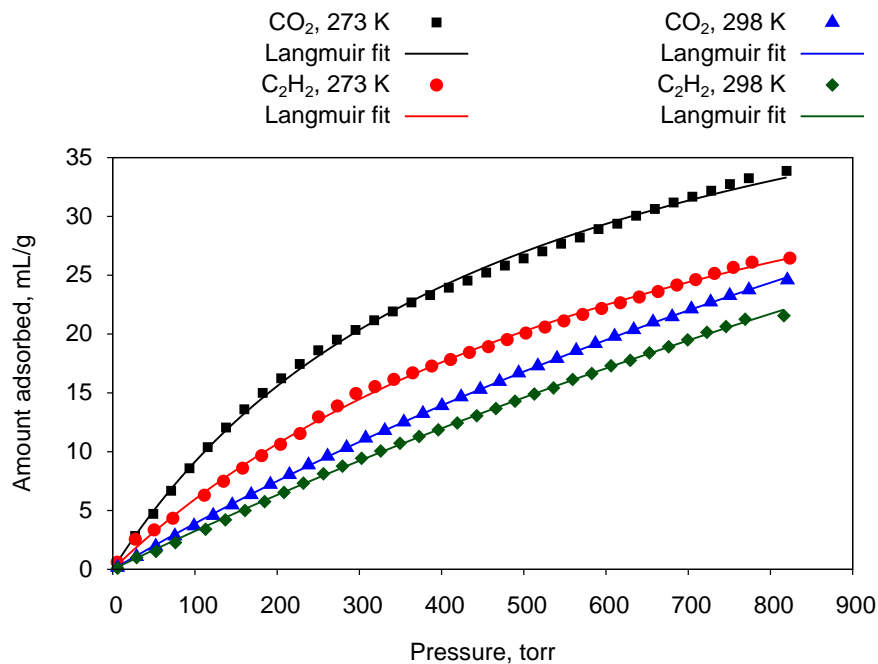


Figure S24. Fits of isotherms by Langmuir equation.

Henry constants (Table S10) were calculated using virial coefficients by equation (S5):

$$K_h = \exp \left[\frac{-A_0}{T} - B_0 \right] \quad (\text{S5})$$

Table S10. Henry constants for gas adsorption on **Eu-MOF** in mmol·g⁻¹·bar⁻¹ at 273 K and 298 K.

Gas\Temperature	273 K	298 K
C ₂ H ₂	2.730	0.995
CO ₂	4.066	1.274